IAEA nuclear fusion

Overview of the first Wendelstein 7-X long pulse campaign with fully water-cooled plasma facing components

To cite this article: O. Grulke *et al* 2024 *Nucl. Fusion* **64** 112002

OPEN ACCESS
IOP Publishing | International Atomic Energy Agency
Nuclear Fusion
Nucl. Fusion **64** (2024) 112002 (10pp)
https://doi.org/10.1088/1741-4326/ad2f4d

Overview of the first Wendelstein 7-X long pulse campaign with fully water-cooled plasma facing components

O. Grulke[1,25,a,*], C. Albert[2], J.A. Alcuson Belloso[1], P. Aleynikov[1], K. Aleynikova[1], A. Alonso[3], G. Anda[4], T. Andreeva[1], M. Arvanitou[10], E. Ascasibar[3], E. Aymerich[5], K. Avramidis[48], J.-P. Bähner[6], S.-G. Baek[6], M. Balden[7], J. Baldzuhn[1], S. Ballinger[6], M. Banduch[1], S. Bannmann[1], A. Bañón Navarro[7], L. Baylor[8], C.D. Beidler[1], M. Beurskens[1], C. Biedermann[1], G. Birkenmeier[7], T. Bluhm[1], D. Boeckenhoff[1], D. Boeyaert[9], D. Bold[1], M. Borchardt[1], D. Borodin[11], H.-S. Bosch[1,10], H. Bouvain[1], S. Bozhenkov[1], T. Bräuer[1], H. Braune[1], C. Brandt[1], S. Brezinsek[11,13], K.J. Brunner[1], C. Büschel[1], R. Bussiahn[1], A. Buzás[4], B. Buttenschoen[1], V. Bykov[1], I. Calvo[3], A. Cappa[3], F. Carovani[1], D. Carralero[3], A. Carls[1], B. Carvalho[12], D. Castaño-Bardawil[15], N. Chaudhary[1], I. Chelis[48], S. Chen[1,10], D. Cipciar[1], J.W. Coenen[11], G. Conway[7], M. Cornelissen[1,27], Y. Corre[14], P. Costello[1], K. Crombe[15,24], G. Cseh[4], B. Csillag[4], H.I. Cu Castillo[7], G. Czymek[11], H. Damm[1], R.J. Davies[1], C. Day[16], S. Degenkolbe[1], R. De Wolf[17], W. Dekeyser[17], A. Demby[9], P. Despontin[15], C.P. Dhard[1], A. Dinklage[1,18], F.A. d'Isa[19], T. Dittmar[11], M. Dreval[20], M. Drevlak[1], P. Drews[11], J. Droste[18], D. Dunai[4], C. Dyhring[10], P. van Eeten[1], E. Edlund[21], M. Endler[1], D.A. Ennis[22], F.J. Escoto[3], M.S. Espinosa[1,10], T. Estrada[3], D. Fehling[8], L. Feuerstein[16], J. Fellinger[1], Y. Feng[1], D.L.C. Fernando[7], S. Fischer[1], E.R. Flom[9], O. Ford[1], T. Fornal[23], J. Frank[1,10], H. Frerichs[9], G. Fuchert[1], G. Gantenbein[16], Y. Gao[1], K. Garcia[9], I. García-Cortés[3], J.M. García-Regaña[3], B. Geiger[9], J. Geiger[1], P. Geissler[1,18], M. Gerard[9], G. Godino-Sedano[3], T. Gonda[22], A. González[3], A. Goriaev[15], D. Gradic[1], M. Grahl[1], H. Greuner[7], E. Grigore[50], M. Gruca[23], J.F. Guerrero Arnaiz[1], V. Haak[1], L. van Ham[1], K. Hammond[26], B. Hamstra[27], X. Han[9], S.K. Hansen[6], J. Harris[8], D. Hartmann[1], D. Hathiramani[1], S. Hegedus[4], S. Heinrich[1], P. Helander[1,18], F. Henke[1], S. Henneberg[1], L. Henschke[1], M. Hirsch[1], U. Hoefel[1], K. Hoefler[7], S. Hoermann[7,42], K.-P. Hollfeld[51], A. Holtz[1], D. Höschen[11], M. Houry[14], J. Huang[11], J. Huang[11], M. Hubeny[11], K. Hunger[7], D. Hwangbo[45], K. Ida[28], Y. Igitkhanov[16], S. Illy[16], Z. Ioannidis[48], M. Jablczynska[23], S. Jablonski[23], B. Jabłoński[29], B. Jagielski[1], M. Jakubowski[1], J. Jelonnek[16], F. Jenko[7], J. Jin[16], A. Johansson[1], G. Jouniaux[15], S. Kajita[30], J.-P. Kallmeyer[1], U. Kamionka[1], W. Kasparek[49], C. Kawan[11], Ye. O. Kazakov[15], N. Kenmochi[28], W. Kernbichler[2], A.K. Kharwandikar[1], M. Khokhlov[1], C. Killer[1], A. Kirschner[11], R. Kleiber[1], C.C. Klepper[8], T. Klinger[1,18], J. Knauer[1], A. Knieps[11], M. Kobayashi[28], G. Kocsis[4], Y. Kolesnichenko[31], A. Könies[1], J. Kontula[32], P. Kornejew[1], S.A. Korteweg[27], J. Koschinsky[1], J. Koster[1,10], Y. Kovtun[20], A. Krämer-Flecken[11], M. Krause[1], T. Kremeyer[1], L. Krier[16], D.M. Kriete[22], M. Krychowiak[1], I. Książek[33], M. Kubkowska[23], M.D. Kuczyński[1], D. Kulla[1], A. Kumar[34], T. Kurki-Suonio[32], I. Kuzmych[35], S. Kwak[1], V. Lancelotti[15], A. Langenberg[1], H. Laqua[1], H.P. Laqua[1,18], M.R. Larsen[25],

---

[a] Present address: MPI for Plasma Physics, Wendelsteinstr. 1, 17491 Greifswald, Germany.

[*] Author to whom any correspondence should be addressed.

1741-4326/24/112002+10$33.00 Printed in the UK

S. Lazerson[1], C. Lechte[49], B. Lee[26], A. LeViness[26], M. Lewerentz[1], Y. Liang[11], L. Liao[11], A. Litnovsky[11,36], J. Liu[11], J. Loizu[37], R. Lopez-Cansino[38], L.D. Lopez Rodriguez[15,24], A. Lorenz[1], R. Lunsford[26], Y. Luo[11], V. Lutsenko[31], N. Maaziz[1], M. Machielsen[37], R. Mackenbach[27], D. Makowski[29], E. Maragkoudakis[3], O. Marchuk[11], M. Markl[2], S. Marsen[1], J. Martínez[3], N. Marushchenko[1], S. Masuzaki[28], D.A. Maurer[22], M. Mayer[7], K.J. McCarthy[3], P. McNeely[1], D. Medina Roque[3], J. Meineke[1], S. Meitner[8], S. vaz Mendes[1], A. Menzel-Barbara[1], B. van Milligen[3], A. Mishchenko[1], V. Moiseenko[47], A. Möller[1], S. Möller[11], D. Moseev[1], G. Motojima[28], S. Mulas[3], P. Mulholland[27], M. Nagel[1], D. Nagy[4], Y. Narbutt[1], D. Naujoks[1], P. Nelde[1,10], R. Neu[7], O. Neubauer[11], U. Neuner[1], D. Nicolai[11], S. Nielsen[25], C. Nührenberg[1], R. Ochoukov[7], G. Offermanns[51], J. Ongena[15], J.W. Oosterbeek[1], M. Otte[1], N. Pablant[26], N. Panadero Alvarez[3], A. Pandey[1], G. Partesotti[1], E.A. Pasch[1], R. Pavlichenko[20], E. Pawelec[33], T.S. Pedersen[1], V. Perseo[1], B. Peterson[28], F. Pisano[5], B. Plaum[49], G. Plunk[1], L. Podavini[1], N.S. Polei[18], P. Poloskei[1], S. Ponomarenko[1], P. Pons-Villalonga[3], M. Porkolab[6], J. Proll[27], M.J. Pueschel[27,39], A. Puig Sitjes[1], R. Ragona[25], K. Rahbarnia[1], M. Rasiński[11], J. Rasmussen[25], D. Refy[4], F. Reimold[1], M. Richou[14], J.S. Riemann[1], K. Riße[1], J. de la Riva Villén[3], G. Roberg-Clark[1], E. Rodriguez[1], V. Rohde[7], J. Romazanov[11], T. Romba[1], D. Rondeshagen[1], M. Rud[25], T. Ruess[16], T. Rummel[1], A. Runov[1], C. Ruset[50], N. Rust[1], L. Ryc[23], T. Rzesnicki[16], M. Salewski[25], E. Sánchez[3], L. Sanchis Sanchez[32], G. Satheeswaran[11], J. Schacht[1], E. Scharff[1], J. Schilling[1], G. Schlisio[1], K. Schmid[7], J.C. Schmitt[22], O. Schmitz[9], M. Schneider[1], M. Van Schoor[15], T. Schröder[1], R. Schroeder[1], B. Schweer[15], S. Sereda[9], B. Shanahan[1], G. Sias[5], S. Simko[9], L. Singh[9], Y. Siusko[20], C. Slaby[1], M. Ślęczka[40], B.S. Smith[25], D.R. Smith[9], H. Smith[1], M. Spolaore[41], A. Spring[1], T. Stange[1], A. von Stechow[1], I. Stepanov[15], M. Stern[1], U. Stroth[7,42], Y. Suzuki[43], C. Swee[9], L. Syrocki[23], T. Szabolics[4], T. Szepesi[4], R. Takacs[4], H. Takahashi[44], N. Tamura[28], C. Tantos[16], J. Terry[6], S. Thiede[1], H. Thienpondt[3], H. Thomsen[1], M. Thumm[16], T. Thun[1], S. Togo[45], T. Tork[1], H. Trimino Mora[1], A. Tsikouras[27], Y. Turkin[1], L. Vano[1], S. Varoutis[16], M. Vecsei[1], J.L. Velasco[3], M. Verstraeten[15], M. Vervier[15], E. Viezzer[38], J. Wagner[1], E. Wang[11], F. Wang[11], M. Wappl[1], F. Warmer[27], T. Wegner[1], Y. Wei[11], G. Weir[1], N. Wendler[23], U. Wenzel[1], A. White[6], F. Wilms[7], T. Windisch[1], A. Winter[1], V. Winters[1], R. Wolf[1,10], G. Wurden[46], P. Xanthopoulos[1], H.M. Xiang[11], S. Xu[11], H. Yamada[30], J. Yang[11], R. Yi[11], M. Yokoyama[28], B. Zamorski[40], M. Zanini[1], M. Zarnstorff[26], D. Zhang[1], S. Zhou[11], J. Zhu[1], J. Zimmermann[18], A. Zocco[1] and S. Zoletnik[4]

[1] Max-Planck Institute for Plasma Physics, Wendelsteinstrasse 1, 17491 Greifswald, Germany
[2] Fusion@OEAW, Graz University of Technology, Petersgasse 16, 8010 Graz, Austria
[3] CIEMAT, Avenida Complutense, 40, 28040 Madrid, Spain
[4] HUN-REN Centre for Energy Research, Konkoly-Thege út 29-33, 1121 Budapest, Hungary
[5] University of Cagliari, Via Università, 40, 09124 Cagliari, Italy
[6] Massachusetts Institute of Technology, 77 Massachusetts Ave, Cambridge, MA 02139, United States of America
[7] Max-Planck-Institute for Plasma Physics, Boltzmannstraße 2, 85748 Garching bei München, Germany
[8] Oak Ridge National Laboratory, 1 Bethel Valley Rd, Oak Ridge, TN 37830, United States of America
[9] University of Wisconsin-Madison, Engineering Drive, Madison, WI 53706, United States of America
[10] Technical University of Berlin, Strasse des 17. Juni 135, 10623 Berlin, Germany
[11] Forschungszentrum Jülich GmbH, Institut fur Energie und Klimaforschung / Plasmaphysik (IEK-4), TEC Partner, 52425 Jülich, Germany
[12] Instituto de Plasmas e Fusao Nuclear, Av. Rovisco Pais, 1049-001 Lisboa, Portugal
[13] Faculty of Mathematics and Natural Sciences, Heinrich Heine University Düsseldorf, 40225 Düsseldorf, Germany
[14] CEA Cadarache, 13115 Saint-Paul-lez-Durance, France
[15] Laboratory for Plasma Physics, LPP-ERM/KMS, TEC Partner, B-1000 Brussels, Belgium
[16] Karlsruhe Institute of Technology, Kaiserstr. 12, 76131 Karlsruhe, Germany
[17] KU Leuven, Celestijnenlaan 300 - box 2421, Leuven 3001, Belgium

[18] Insitute of Physics, University of Greifswald, Felix-Hausdorff-Str. 6, 17489 Greifswald, Germany
[19] ENEA—Centro Ricerche Frascati, Via Enrico Fermi, 45, 00044 Frascati RM, Italy
[20] Institute of Plasma Physics, National Science Center 'Kharkiv Institute of Physics and Technology', Kharkiv, Ukraine
[21] SUNY Cortland, Cortland, NY, United States of America
[22] Auburn University, Auburn, AL 36849, United States of America
[23] Institute of Plasma Physics and Laser Microfusion, 23 Hery Str., 01-497 Warsaw, Poland
[24] Department of Applied Physics, Ghent University,Sint-Pietersnieuwstraat 41 B4 9000 Ghent, Belgium
[25] Technical University of Denmark, Department of Physics, Anker Engelunds Vej, 2800 Kgs Lyngby, Denmark
[26] Princeton Plasma Physics Laboratory, Princeton, NJ 08543, United States of America
[27] Eindhoven University of Technology, 5600 MB Eindhoven, Netherlands
[28] National Institute for Fusion Science, National Institutes of Natural Sciences, 322-6 Oroshi-cho, Toki, Gifu Prefecture 509-5292, Japan
[29] Lódź University of Technology, Department of Microelectronics and Computer Science, Wólczańska 221, 93-005 Lódź, Poland
[30] University of Tokyo, 5-1-5 Kashiwanoha, Kashiwa, Chhiab 277-0882 Japan
[31] Institute for Nuclear Research, prospekt Nauky 47, Kyiv 03028, Ukraine
[32] Aalto University, 02150 Espoo, Finland
[33] University of Opole, plac Kopernika 11a, 45-001 Opole, Poland
[34] The Australian National University, Acton ACT 2601, Canberra, Australia
[35] Karazin Kharkiv National University, Svobody Square, 4, Kharkiv, Kharkiv Oblast 61000 Ukraine
[36] National Research Nuclear University MEPhI, 115409 Moscow, Russian Federation
[37] École Polytechnique Fédérale de Lausanne, Swiss Plasma Center, CH-1015 Lausanne, Switzerland
[38] Dept. of Atomic, Molecular and Nuclear Physics, Universidad de Sevilla, Sevilla 41012, Spain
[39] Dutch Institute for Fundamental Energy Research, PO Box 6336, 5600 HH Eindhoven, Netherlands
[40] Institute of Physics, University of Szczecin, al. Papieża Jana Pawła II 22A, 70-453 Szczecin, Poland
[41] Consorzio RFX, Corso Stati Uniti, 4, 35127 Padova, Italy
[42] Technical University of Munich, TUM School of Natural Sciences, Physics Department, 85748 Garching, Germany
[43] Graduate School of Advanced Science and Engineering, Hiroshima University, 739-8527 Higashi-Hiroshima, Japan
[44] Department of Quantum Science and Energy Engineering, Tohoku University, 6-6-01-2, Aza-Aoba, Aramaki, Aoba Ward, Sendai, Miyagi 980-8579, Japan
[45] University of Tsukuba, 1-1-1 Tennodai, Tsukuba, Ibaraki 305-8577, Japan
[46] Los Alamos National Laboratory, NM 87545, United States of America
[47] Division for Electricity, Uppsala University, Box 65, 751 03 Uppsala, Sweden
[48] Department of Physics, National and Kapodistrian University of Athens, Zografou University Campus, 15784 Athens, Greece
[49] Institute for Interfacial Process Engineering and Plasma Technology, University of Stuttgart, 70569 Stuttgart, Germany
[50] National Institute for Laser, Plasma and Radiation Physics, PO Box MG-36, Magurele-Buchares, Romania
[51] Forschungszentrum Jülich GmbH, Zentralinstitut fur Elektronik und Analytik (ZEA-1), 52425 Jülich, Germany

E-mail: grulke@ipp.mpg.de

Received 8 December 2023, revised 30 January 2024
Accepted for publication 1 March 2024
Published 15 August 2024

Abstract

After a long device enhancement phase, scientific operation resumed in 2022. The main new device components are the water cooling of all plasma facing components and the new water-cooled high heat flux divertor units. Water cooling allowed for the first long-pulse operation campaign. A maximum discharge length of 8 min was achieved with a total heating energy of 1.3 GJ. Safe divertor operation was demonstrated in attached and detached mode. Stable detachment is readily achieved in some magnetic configurations but requires impurity seeding in configurations with small magnetic pitch angle within the edge islands. Progress was made in the characterization of transport mechanisms across edge magnetic islands: Measurement of the potential distribution and flow pattern reveals that the islands are associated with a strong poloidal drift, which leads to rapid convection of energy and particles from the last closed flux surface into the scrape-off layer. Using the upgraded plasma heating systems, advanced heating scenarios were developed, which provide improved energy confinement comparable to the scenario, in which the record triple product for stellarators was achieved in the previous operation campaign. However, a magnetic configuration-dependent critical heating power limit of the electron cyclotron resonance heating was observed. Exceeding the respective power limit leads to a degradation of the confinement.

Keywords: stellarator, long-pulse operation, magnetic fusion confinement, divertor detachment

1. Introduction

The main scientific objective of the superconducting stellarator Wendelstein 7-X (W7-X) is to lay the physics foundation to scale advanced stellarator concepts to a Helical-Axis Advanced Stellarator (HELIAS) type reactor design [1]. The modeling-driven optimization of the W7-X magnetic field configuration is expected to provide considerably improved neoclassical and fast ion confinement, magneto-hydrodynamic stability at high plasma-β and a feasible exhaust concept with the implementation of an island divertor [2, 3]. The neoclassical optimization has already been experimentally verified [4], particularly with respect to the considerable reduction of the neoclassical transport when compared to classical stellarator configurations [5]. W7-X has undergone a number of device modifications. Starting with first plasma operation in limiter configuration in 2015 (operation phase OP 1.1), an inertially-cooled graphite test divertor module was installed for the second experimental campaign (operation phase OP 1.2) conducted in 2017/2018 and the concept of the island divertor was successfully demonstrated in attached and detached operation [6–8]. In these two initial experimental campaigns the energy turnaround in the plasma was strongly limited due to the lack of cooling of the plasma facing components and the heating energy could not exceed 200 MJ. During a long operation pause 2018–2021, the device was technically enhanced with the installation of the water cooling of all plasma facing components and the installation of the fully water-cooled high heat flux divertor modules [9], which is the pre-requisite to achieve the project goal to demonstrate steady-state long-pulse operation of up to 30 min plasma duration at a heating power of 10 MW, resulting in an energy turnaround of 18 GJ. After a long device commissioning period in the first half of 2022, scientific operation resumed and the operation campaign OP 2.1 was conducted in the period September 2022–March 2023. In total 1700 plasma discharges were conducted in a wide range of plasma parameters and magnetic configurations. The priorities of the OP 2.1 scientific program stem from three main objectives: (i) demonstration of long-pulse operation, (ii) safe divertor operation and (iii) development of advanced heating and confinement scenarios. The strategy for long-pulse operation of W7-X reaching 18 GJ energy turnaround is to increase the heating energy over the next operation campaigns gradually. For OP 2.1 a milestone of 1 GJ energy turnaround was defined. The new high heat flux divertor modules have a much more strict temperature limit and safe divertor operation with control of the strike line position is of paramount importance. The scientific program focused on studies of attached and detached divertor scenarios. Exceptional confinement scenarios were already developed in the second operation campaign OP 1.2, in which a record triple product for stellarators was transiently achieved [10]. An important objective was to continue these studies and to develop alternative scenarios using the upgraded plasma heating systems. The Electron Cyclotron Resonance (ECR) heating systems could be operated up to a maximum power of 6.5 MW in second harmonic X- and O-polarization (X2 and O2). The upgraded Neutral Beam Injection (NBI) system allowed for the operation of up to three injectors with an injected power of 2 MW per injector. This paper gives an overview of the main achievements of the recent experimental campaign OP 2.1. In section 2 the operation of the cooled high heat flux divertor and long pulse operation are addressed. The achievements and progress of detached divertor operation are outlined in section 3. Advanced heating scenarios are presented in section 4, before results are briefly summarized in section 5.

2. Preparation for long pulse operation and long pulse scenarios

The key components of the recent major W7-X device modifications were the completion of the in-vessel water cooling manifold supplying all plasma facing components and in-vessel diagnostics systems and the new water-cooled high heat flux divertor modules. As displayed in figure 1(*a*), approximately 600 water cooling circuits were installed entering the vacuum vessel. Intense Helium leak testing during the installation steps of the water manifold ensured tightness and no water leaks occurred throughout the entire operation campaign. The individual sub-circuits were hydraulically balanced to provide the nominal water flow rate through each in-vessel component. One high heat flux divertor module is displayed in figure 1(*b*). The divertor surface and baffle geometry remained unchanged when compared to the previously operated inertially cooled divertor. However, due to its water cooling the

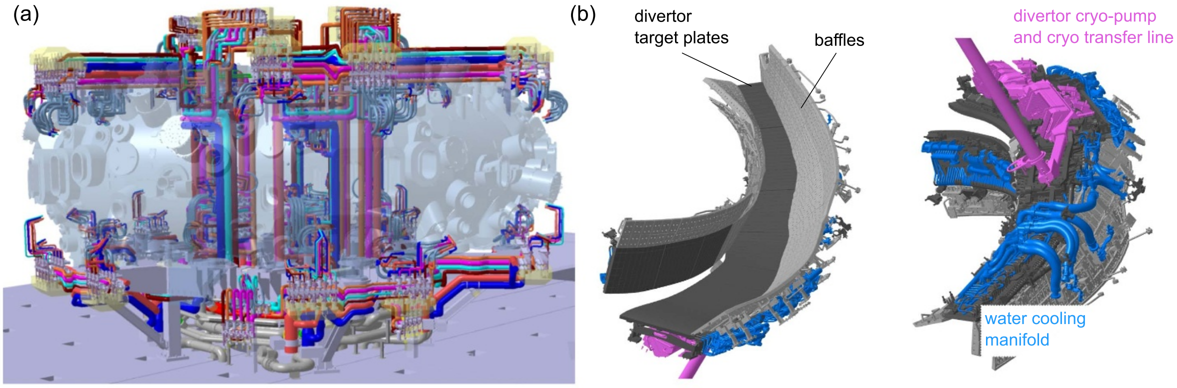

Figure 1. (*a*) Overview of the water manifold installation for the cooling of plasma facing components. (*b*) The newly installed high heat flux divertor with its baffles, cooling manifold and cryogenic pump.

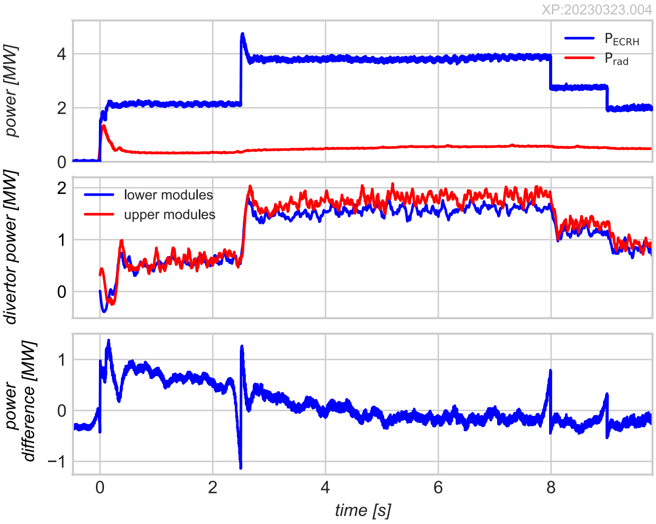

Figure 2. Plasma discharge with ECR heating power steps and plasma radiation power (top), the associated integral power exhausted by the upper and lower divertor modules, respectively (middle), and the difference $P_{\mathrm{heat}} - P_{\mathrm{rad}} - P_{\mathrm{div}}$.

divertor is specified for a steady-state power density of up to $10\,\mathrm{MW\,m^{-2}}$ [11]. In addition to the water-cooled structure, each divertor module is equipped with a cryogenic pumping system, installed underneath the pumping gap, with a maximum pumping capacity of $70\,\mathrm{m^3\,s^{-1}}$. The divertor steady-state heat load specification aligns with the W7-X goal to demonstrate long-pulse operation with plasma heating power of 10 MW, but requires the power loads to be symmetrically distributed over all divertor modules, corresponding to a strike line area of $1\,\mathrm{m^2}$. The symmetrization entails an accurate mechanical alignment of the divertor modules and correction of magnetic error fields with the auxiliary magnetic coil systems [12]. The resulting divertor power loads are displayed exemplary in figure 2 for a pure ECR heated plasma with a maximum heating power of 4 MW and divertor attachment. The radiated power is small throughout the discharge with $P_{\mathrm{rad}} < 1$ MW. A comparison of the integral power load at the upper and lower divertor modules shows that indeed the power is highly symmetrically distributed across all divertor modules. Moreover, equating the heating power with the divertor power, taking the radiated power into consideration $P_{\mathrm{heat}} - P_{\mathrm{rad}} - P_{\mathrm{div}}$, shown in the lower panel of figure 2, reveals that almost all power is exhausted via the divertor target plates. Only in the initial lower density phase, the power difference is transiently larger. Convective loads to other plasma facing components represent only a minor fraction of typically less than $10\%P_{\mathrm{heat}}$. From the observed divertor temperatures, the power load density to the divertor is estimated using a heat diffusion solver [13, 14]. A maximum power load density to the divertor modules of $6\,\mathrm{MW\,m^{-2}}$ could be demonstrated resulting in moderate divertor surface temperatures of 500 °C, which equilibrates after a time of 4–5 s and is in good agreement with Finite Element Method (FEM) heat load calculations. Based on the proper cooling behavior of the high heat load divertor, the first long-pulse operation could be conducted. As a precaution a maximum heating energy of 1 GJ was defined for the last operation campaign. As displayed in figure 3, a purely ECR heated plasma at a moderate power level of maximum $P_{ECRH} = 3$ MW with an attached divertor was operated with a total discharge length of 480 s. A shallow plasma density ramp was programmed to counterbalance potential impurity radiation at later times in the discharge. This has, however, not posed to be any issue. Due to technical problems and drop out of individual gyrotrons in the second half of the discharge, starting at 300 s, the associated drop in electron temperature leads to a step-wise reduction of the diamagnetic energy and bootstrap current. Nevertheless, a total heating energy of 1.3 GJ could be achieved. The maximum divertor surface temperature with $T_{\mathrm{surface}} < 650\,^{\circ}\mathrm{C}$ at the strike line remains well below the specified maximum temperature of $T_{\mathrm{max}} = 1200\,^{\circ}\mathrm{C}$. The heat load onto the divertor can be further reduced by operating long-pulse discharges with divertor detachment. A proof of principle plasma discharge is shown in figure 4. After a plasma startup phase with increased ECR heating power, the discharge remains stationary for a total length of 110 s at an ECR heating power of $P_{ECRH} = 4$ MW and high plasma density of $n = 1 \cdot 10^{20}\,\mathrm{m^{-3}}$. Detachment is supported by the feed-forward seeding of Neon gas puffs every 2 s, which stabilizes the radiated power fraction

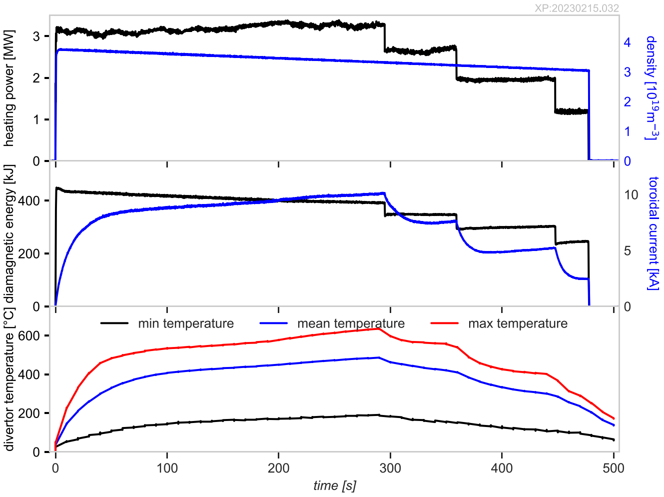

Figure 3. Time traces of the long pulse scenario with a total discharge length of 480 s: ECR heating power and mean plasma density (top), diamagnetic energy and toroidal bootstrap current (middle), and the divertor surface temperature (bottom).

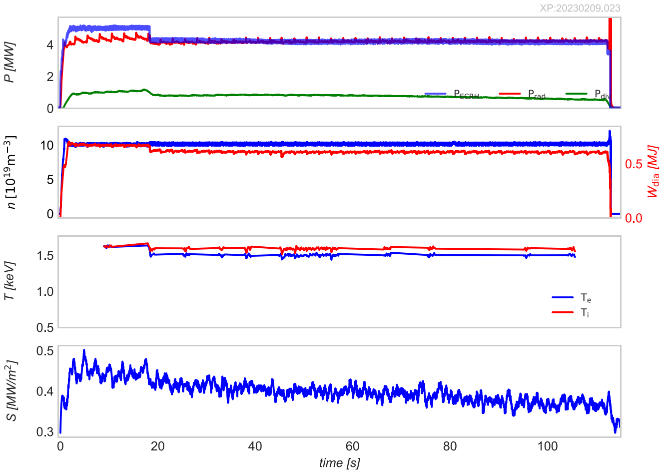

Figure 4. Time traces of a long discharge with full divertor detachment: ECR heating power, (*a*) plasma radiation power and power arriving at the divertor, (*b*) plasma density and diamagnetic energy, (*c*) electron and ion temperature, (*d*) power density at the divertor surface.

to $P_{\mathrm{rad}} \geqslant 0.8P_{ECRH}$. At the high plasma densities, electrons and ions are well coupled at a temperature of $T_e = T_i = 1.5$ keV. The power density at the divertor surfaces remain well below 1 MW m^{-2}.

3. Divertor detachment and island transport

In general, scenarios with divertor detachment in W7-X are not only achieved via impurity seeding, but the intrinsic carbon radiation at high plasma densities is sufficient. An example plasma discharge is displayed in figure 5, in which at constant ECR heating power of $P_{ECRH} = 4.5$ MW the plasma density is increased in two steps from initially $n = 9 \cdot 10^{19}$ m^{-3} to $n = 1.2 \cdot 10^{20}$ m^{-3} and finally $n = 1.4 \cdot 10^{20}$ m^{-3}. The plasma radiation, which is initially relatively small with $P_{rad} \approx 0.25P_{ECRH}$ increases accordingly to $0.65P_{ECRH}$ and finally to $>0.9P_{ECRH}$. The radiation is localized to the divertor region and the diamagnetic energy only mildly responds to the increased radiation. Due to the strong electron to ion coupling, the electron temperature equilibrates with the ion temperature, which remain rather constant throughout the entire discharge. During the density steps, the divertor state transitions from a fully attached divertor with significant heat flux densities of up to 3 MW m^{-2}, via a partially detached divertor to full detachment with heat flux densities $\ll 1$MW m^{-2}. The transition to divertor detachment is accompanied by a gradual increase of the neutral particle pressure in the sub-divertor region. It should be noted, however, that the achieved neutral compression in the sub-divertor region has not been large enough, yet, to allow for effective cryo pumping. Inspection of the time traces of plasma density, radiated power, and neutral density reveals the onset of fluctuations of plasma density, radiated power and sub-divertor pressure in the full detachment phase. It is found that these fluctuations show a strong dependence on the edge magnetic configuration. This behavior is shown in figure 6 for two configurations differing in the edge rotational transform, $\iota\!\!\!- = 5/5$ and $\iota\!\!\!- = 5/6$. The main difference in these two cases are the different magnetic connection lengths to the divertor target plates, which in the $5/6$ configuration are typically $600 - 1000$ m compared to $300 - 500$ m in the $5/5$ case. In both cases, plasma discharges at identical heating powers and densities were performed, leading to divertor detachment. In the $5/5$ situation, detachment is stable, whereas in the $5/6$ case similar fluctuations in plasma density and radiative power are observed as in figure 5, leading to a premature end via a radiative collapse. The most striking difference is the localization of edge radiation. The carbon radiation pattern for $\iota\!\!\!- = 5/6$ as obtained from EMC3-EIRENE simulations and shown in figure 6(*b*) and experimentally observed via bolometry shows the clear signature of strong radiation from the O-point region of the magnetic islands. This stands in contrast to the $5/5$ case, in which most of the radiation is observed in the island's X-point region [15]. Since the radiation is strongly dependent on the electron temperature, these results strongly suggest a different energy transport within the magnetic islands. This is indeed expected since the ratio of parallel to perpendicular energy and particle transport scales as the magnetic pitch angle within the magnetic island $\Gamma_{\|}/\Gamma_{\perp} \sim \theta^2$ [16], which is significantly smaller in the $5/6$ configuration due to its higher poloidal mode number and decreased magnetic shear. The detachment stability of the $5/6$ configuration improves with seeding of impurities that exhibit peak radiation at higher temperatures (e.g. Neon). Both simulation and experiment show a broader spatial distribution of the radiation zone in this case as compared with intrinsic carbon, suggesting that the detachment instability is related to specifics of the radiation cooling efficiency of the impurity. However, research into the stability analysis is preliminary and further experimental and simulation work is required. Thus, a quantitative understanding of the radiation characteristics within magnetic islands requires an understanding of the island's transport processes. The dependence of the perpendicular transport on the magnetic pitch angle only takes diffusive processes into account.

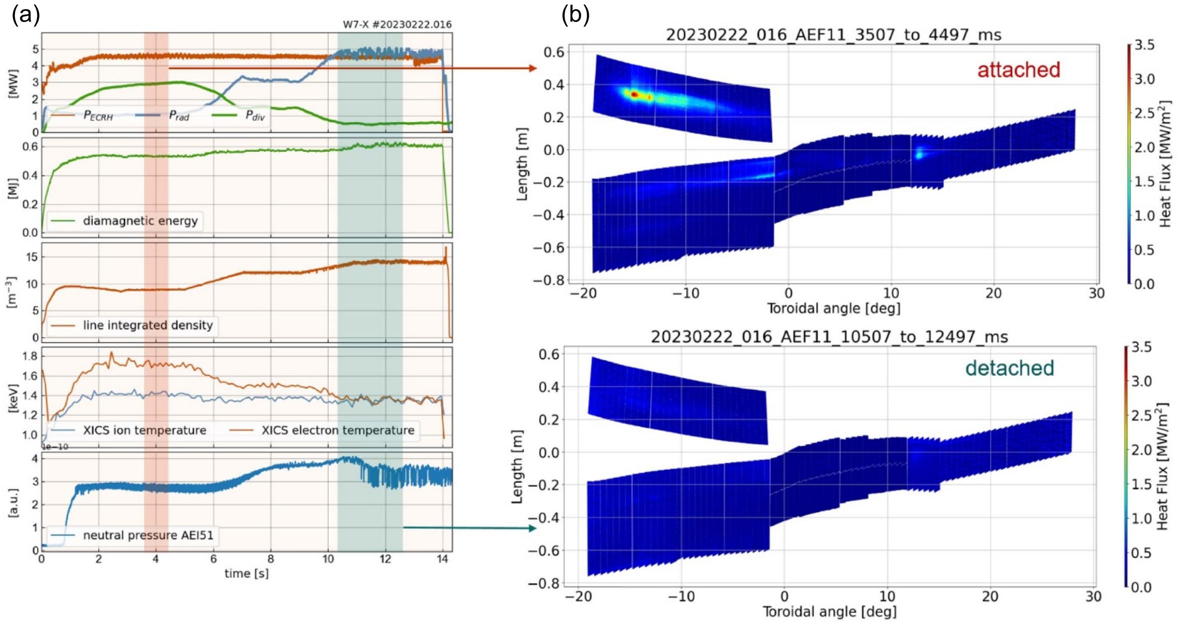

Figure 5. Transition from attached to detached divertor showing (*a*) time traces of ECR heating power P_{ECRH}, radiated power P_{rad} and power to the divertor P_{div}, diamagnetic energy, line integrated density, electron and ion temperatures and the neutral gas pressure in the sub-divertor region, (*b*) IR measurements of the divertor surface temperature for the attached and detached phase marked in the time traces.

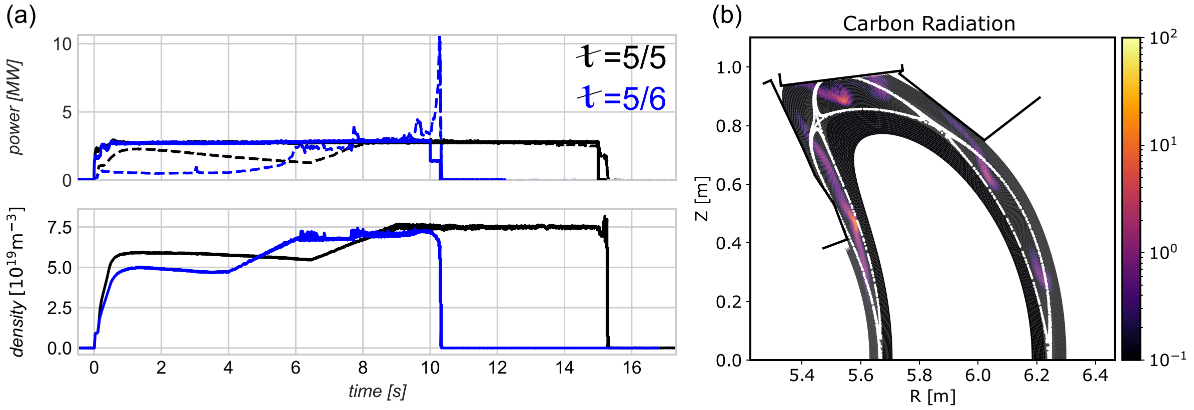

Figure 6. Comparison of divertor detachment in two magnetic field configurations with different edge rotational transform, where the ECR heating power is shown as solid, the radiated power as dashed lines in (*a*). Color-coded plot of the EMC3-EIRENE simulation results of the carbon radiation intensity (in arbitrary units) in a poloidal cross section of the 5/6 configuration are shown in (*b*). The island separatrices are superimposed as white lines.

However, new investigations reveal the contribution of convective transport processes within the magnetic island. It has been shown that turbulent transport plays only a minor role in perpendicular island transport, particularly due to the absence of large quasi-ballistic perpendicular filament transport over large radial distances [17]. Measurement of the electric potential distribution within an island using electric probes and shown in figure 7(*a*) yield significant radial electric field (perpendicular to the closed island magnetic flux surfaces). The potential profiles depend strongly on the magnetic connection lengths to the divertor target plates but remains peaked at the island O-point. The associated perpendicular electric fields gives rise to $E \times B$ drifts, which convect particles and energy from the separatrix region into the mid Scrape-Off Layer (SOL) and represent a strong transport channel, which at low to moderate plasma densities typically exceeds the diffusive perpendicular transport by an order of magnitude. The drift velocities as estimated from the potential profiles and shown in figure 7(*b*) are compared to direct measurements of the propagation of plasma fluctuations using the gas-puff imaging diagnostic. Both results are qualitatively and quantitatively consistent and clearly reveal the poloidal plasma flow within the island.

4. High-performance operation

Previous experimental investigations have confirmed that the optimized magnetic geometry of W7-X leads to a reduction of the neoclassical transport when compared to classical

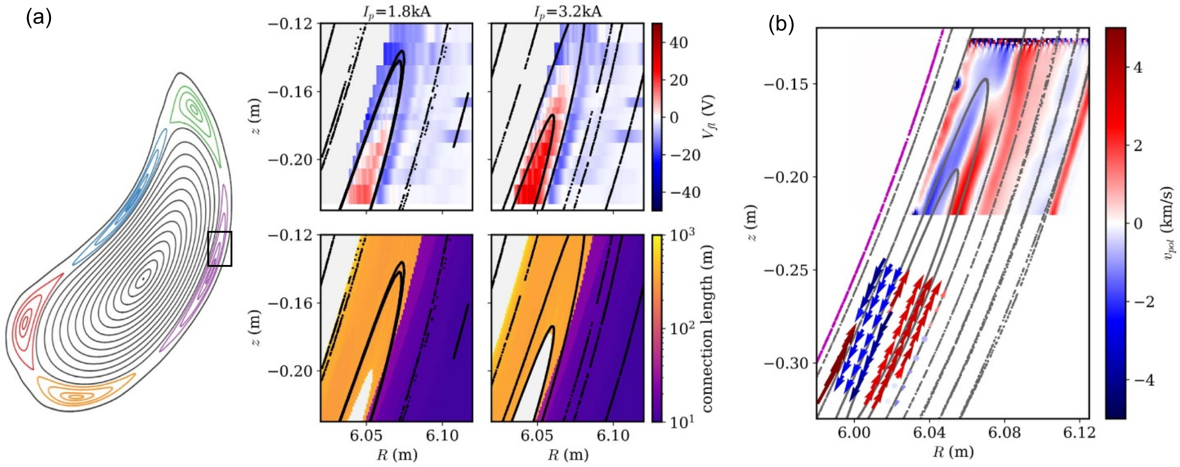

Figure 7. (*a*) Probe measurements of the floating potential in a poloidal cross section covering a part of the outboard midplane magnetic island (indicated in the Poincaré plot to the left) and the respective connection length along the magnetic field to the divertor target plates. The reconstructed poloidal $E \times B$ flow velocity (color-coded) together with direct flow measurements as obtained from GPI measurements (quiver plot) are displayed in (*b*).

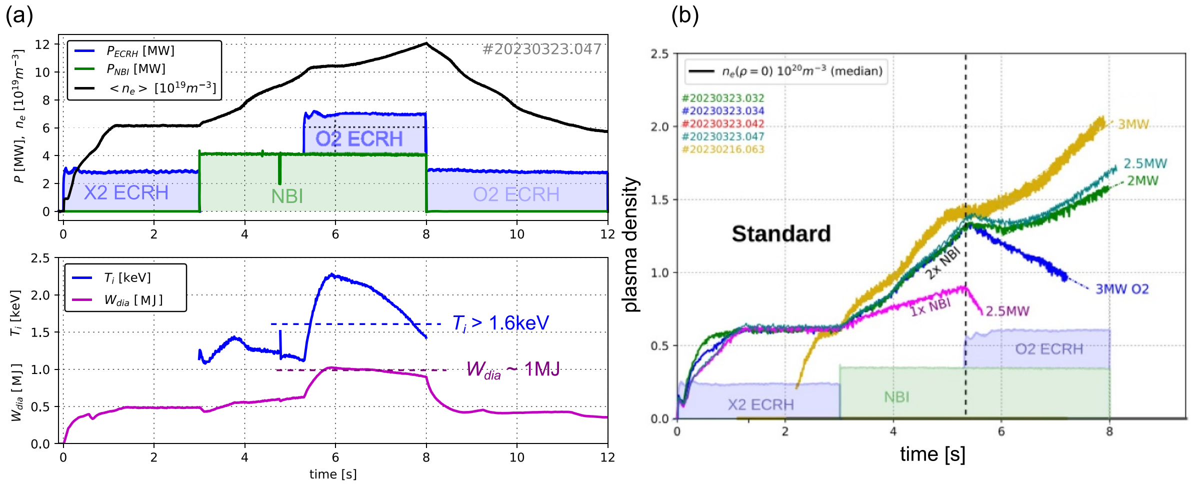

Figure 8. (*a*) Discharge scenario of combined ECR and NBI heating together with the ion temperature T_i and diamagnetic energy W_{dia}. (*b*) comparison of similar discharge scenarios for different combinations of NBI and ECR heating and magnetic field configurations. Here, one or two NBI sources were operated.

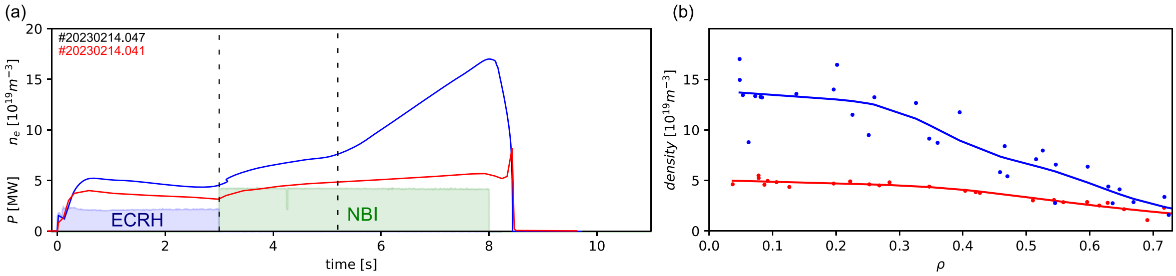

Figure 9. (*a*) Typical time evolution of the central plasma density for pure NBI plasma heating for two different initial ECR heated plasma densities. (*b*) Comparison of the respective radial plasma density profiles.

stellarator geometries [5] and neoclassical transport is generally not the dominant transport mechanisms. Studies of turbulence and transport characteristics strongly suggest that ion temperature gradient turbulence is one of the main candidates determining the ion energy transport in W7-X [18, 19], whereas trapped electron modes and electron gradient turbulence in the magnetic geometry of W7-X are expected to be of minor importance [20, 21]. The enhanced turbulent ion energy transport leads to a rather strict limitation of the achievable peak ion temperature of $T_i \leqslant 1.6$ keV for the heating power available in W7-X [22], often referred to ‘ion temperature clamping’. However, central peaking of the plasma density has been shown to stabilize ion temperature gradient turbulence without the simultaneous de-stabilization of trapped electron turbulence [23] and to provide exceptionally high ion temperatures up to 3 keV, exceeding the clamping limit, and improved energy confinement, considerably exceeding the ISS_{04} confinement scaling [24] by up to 40%. Centrally peaked plasma with improved performance have so far only be realized via pellet fueling and showed an extremely transient nature [25]. In the recent experimental campaign, a different approach was pursued via the combination of ECR and NBI heating, which is depicted in figure 8(*a*). The scenario starts with a conventional ECR heated plasma in X2 polarization, which serves as the target plasma for the NBI heating phase. The ion temperature is consistent with the ion gradient turbulence dominated regime usually observed in purely ECR heated plasmas. The ECR heating is then completely switched off and the discharge is sustained by pure NBI heating. During NBI heating using two injectors providing $P_{NBI} = 4$ MW, the mean plasma density increases. During the pure NBI phase, the ion temperature remains on a similar level. At a mean density of $\approx 1 \cdot 10^{20}\,\mathrm{m}^{-3}$ additional 3 MW of ECR heating in O_2 polarization (to account for the high plasma density) is added, which is accompanied by a sharp increase of the ion temperature reaching $T_i \approx 2.3$ keV, clearly exceeding the clamping limit, with a stored energy reaching $W_{\mathrm{dia}} = 1$ MJ. During the phase of additional ECR heating, the plasma density continues to increase in this case, with an associated drop in ion temperature due to the reducing power per particle. In other cases, with higher ECR heating power, the central density drops rapidly and the turbulence suppression is lost, also causing a drop in ion temperature. Inspection of the effect of pure NBI heating on the radial plasma density profile, shown in figure 9, yields that the typical central plasma density increase displays two phases: in the early phase of NBI heating, a slow increase due to NBI fueling is observed. However, the slope of the density run increases after a few seconds at otherwise constant NBI parameters, indicating a suppression of radial particle transport. However, this plasma density evolution depends on the initial plasma density and does not show any steep central density increase at low starting densities. The corresponding radial density profiles support these observations. For a low initial plasma density, the profile remains flat and no significant influence of NBI heating is observed. However, the steep central density increase corresponds to the development of radial plasma density gradients particularly in the radial range $\rho = 0.2 - 0.5$. In the peaked density profile case, assessments of the radial impurity transport show a reduction to neoclassical level [26]. These observations consolidate the earlier findings using pellet injection that the development of radial density gradients in the confinement region leads to a suppression of turbulent transport, likely due to the stabilization of the ion temperature gradient instability, thereby reducing the radial ion energy transport and leading to increased central ion temperatures. This mechanisms is further supported by the direct observation of electron temperature fluctuations at half plasma radius as measured by the correlation electron cyclotron emission diagnostics, which displays in a similar scenario a clear correlation between the drop of central ion temperature and the rapid increase of turbulent temperature fluctuations, cf figure 10. The duration of the increased ion temperature phase is directly connected to the plasma density profile evolution and is as long as the plasma density remains stationary. However, a systematic study of different combinations of NBI heating power with superimposed additional ECR heating, shown in figure 8(*b*) in different magnetic field configurations suggests a configuration dependent critical ECR heating power. Exceeding this critical ECR heating power leads to a rapid decrease of the plasma density peaking and a loss of the improved confinement. The details of this mechanism are not clear, yet, and require further experimental investigations and kinetic simulation efforts to clarify the role of turbulent transport.

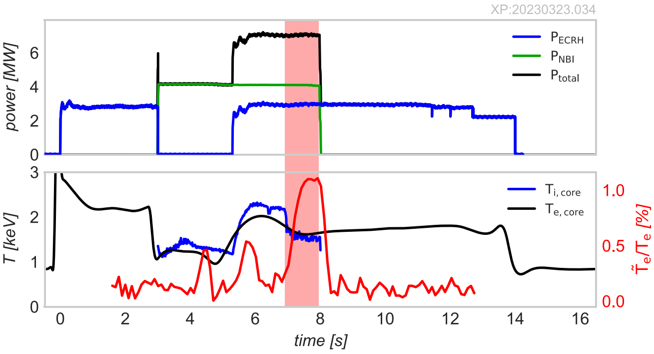

Figure 10. Similar discharge scenario as shown in figure 8 together with measurements of the electron temperature fluctuations $\tilde{T}_e/T_e$.

5. Summary

The technical modifications of W7-X have proved successful. The new water-cooled high heat flux divertor was successfully operated in attached and detached mode. Its temperature evolution was observed within the technical specification, allowing for operation with large steady-state heat flux densities. All 600 water cooling circuits were leak tight and provided the nominal flow rate to the plasma facing components. Long-pulse operation was demonstrated in attached and detached divertor operation. In attached operation a discharge duration of 8 min with an energy turnaround of 1.3 GJ was achieved. Stable detachment was demonstrated for a duration of 110 s with negligible heat flux to the divertor targets. Impurity seeding was found to be indispensable to achieve stable detachment in magnetic configurations with small magnetic pitch angle, i.e. long magnetic connection lengths to the divertor targets, due to the strong localization of intrinsic impurity radiation at the island O-points. Novel diagnostic capabilities provide new insights into the role of drift flows for heat and particle transport in the island divertor SOL. The SOL island structure shows large poloidal drift velocities, which convect plasma from the last closed flux surface into the mid SOL. This mechanism plays a crucial role in perpendicular energy transport processes and the evolution of temperature profiles within the SOL. Advanced heating scenarios were developed using a combination of NBI and ECR heating. Similar to the record confinement scenario of the second operation campaign OP 1.2, central density profile peaking was found to be the key ingredient for enhanced confinement and ion temperatures exceeding the flat density profile limit. However, a configuration-dependent ECR heating power limit was observed. Exceeding the respective limit leads to degeneration of the improved confinement phase.

Acknowledgment

This work has been carried out within the framework of the EUROfusion Consortium, funded by the European Union via the Euratom Research and Training Programme (Grant Agreement No 101052200" EUROfusion). Views and opinions expressed are however those of the author(s) only and do not necessarily reflect those of the European Union or the European Commission. Neither the European Union nor the European Commission can be held responsible for them.

References

[1] Warmer F., Bykov V., Drevlak M., Haeussler A., Fischer U., Stange T., Beidler C.D. and Wolf R.C. (the W7-X Team) 2017 From W7-X to a helias fusion power plant: On engineering considerations for next-step stellarator devices *Fusion Eng. Des.* **123** 47–53

[2] Nuhrenberg J. and Zille R. 1986 Stable stellarators with medium-beta and aspect ratio *Phys. Lett.* A **114** 129–32

[3] Klinger T. *et al* (The Wendelstein 7-X Team) 2017 Performance and properties of the first plasmas of Wendelstein 7-X *Plasma Phys. Control. Fusion* **59** 014018

[4] Dinklage A. *et al* 2018 Magnetic configuration effects on the Wendelstein 7-X stellarator *Nat. Phys.* **14** 855–60

[5] Beidler C.D. *et al* (the W7-X Team) 2021 Demonstration of reduced neoclassical energy transport in Wendelstein 7-X *Nature* **598** E5

[6] Jakubowski M. *et al* (the W7-X Team) 2021 Overview of the results from divertor experiments with attached and detached plasmas at Wendelstein 7-X and their implications for steady-state operation *Nucl. Fusion* **61** 106003

[7] Endler M. *et al* (the W7-X Team) 2021 Wendelstein 7-X on the path to long-pulse high-performance operation *Fusion Eng. Des.* **167** 112381

[8] Krychowiak M. *et al* (the W7-X Team) 2023 First feedback-controlled divertor detachment in W7-X: experience from tdu operation and prospects for operation with actively cooled divertor *Nucl. Mater. Energy* **34** 101363

[9] Bosch H.S., van Eeten P., Grulke O., Braeuer T., Degenkolbe S., Nagel M., Rummel T., Schacht J., Spring A. and Winter A. (W7-X Team) 2023 Preparing the operation of Wendelstein 7-X in the steady-state regime *Fusion Eng. Des.* **193** 113830

[10] Wolf R.C. *et al* (the Wendelstein 7-X Team) 2019 Performance of Wendelstein 7-X stellarator plasmas during the first divertor operation phase *Phys. Plasmas* **26** 082504

[11] Qian X., Peng X., Fellinger J., Boscary J., Bykov V., Wang Z., Ye M. and Song Y. 2016 Assessment of the W7-X high heat flux divertor with thermo-mechanical analysis *Fusion Eng. Des.* **109** 565–8

[12] Lazerson S.A. *et al* (The W7-X Team) 2017 Error field measurement, correction and heat flux balancing on Wendelstein 7-X *Nucl. Fusion* **57** 46026

[13] Herrmann A., Junker W., Gunther K., Bosch S., Kaufmann M., Neuhauser J., Pautasso G., Richter T. and Schneider R. 1995 Energy flux to the ASDEX-Upgrade diverter plates determined by thermography and calorimetry *Plasma Phys. Control. Fusion* **37** 17

[14] Gao Y., Jakubowski M.W., Drewelow P., Pisano F., Sitjes A.P., Niemann H., Ali A. and Cannas B. (W7-X Team) 2019 Methods for quantitative study of divertor heat loads on W7-X *Nucl. Fusion* **59** 066007

[15] Zhang D. *et al* (The W7-X Team) 2021 Bolometer tomography on Wendelstein 7-X for study of radiation asymmetry *Nucl. Fusion* **61** 116043

[16] Feng Y., Kobayashi M., Lunt T. and Reiter D. 2011 Comparison between stellarator and tokamak divertor transport *Plasma Phys. Control. Fusion* **53** 02400

[17] Killer C., Narbutt Y. and Grulke O. (W7-X Team) 2021 Turbulent transport in the scrape-off layer of Wendelstein 7-X *Nucl. Fusion* **61** 096038

[18] Wegner T. *et al* (W7-X team) 2020 Impact of the temperature ratio on turbulent impurity transport in Wendelstein 7-X *Nucl. Fusion* **60** 24004

[19] Baehner J-P. (W7-X Team) 2021 Phase contrast imaging measurements and numerical simulations of turbulent density fluctuations in gas-fuelled ECRH discharges in Wendelstein 7-X *J. Plasma Phys.* **87** 905870314

[20] Proll J.H.E., Helander P., Connor J.W. and Plunk G.G. 2012 Resilience of quasi-isodynamic stellarators against trapped-particle instabilities *Phys. Rev. Lett.* **108** 245002

[21] Plunk G.G. *et al* (the W7-X Team) 2019 Stellarators resist turbulent transport on the electron larmor scale *Phys. Rev. Lett.* **122** 035002

[22] Beurskens M.N.A. *et al* (the W7-X Team) 2021 Ion temperature clamping in Wendelstein 7-X electron cyclotron heated plasmas *Nucl. Fusion* **61** 116072

[23] Alcuson J.A., Xanthopoulos P., Plunk G.G., Helander P., Wilms F., Turkin Y., von Stechow A. and Grulke O. 2020 Suppression of electrostatic micro-instabilities in maximum-j stellarators *Plasma Phys. Control. Fusion* **62** 035005

[24] Yamada H. *et al* 2005 Characterization of energy confinement in net-current free plasmas using the extended international stellarator database *Nucl. Fusion* **45** 1684

[25] Bozhenkov S.A. *et al* (W7-X Team) 2020 High-performance plasmas after pellet injections in Wendelstein 7-X *Nucl. Fusion* **60** 066011

[26] Romba T., Reimold F., Jaspers R.J.E., Ford O.P., Vano L. and Klinger T. (the W7-X Team) 2023 Suppression of anomalous impurity transport in NBI-heated W7-X plasmas *Nucl. Fusion* **63** 076023